ACS Catalysis

Research Article

pubs.acs.org/acscatalysis

Rational Design of High-Performance DeNO$_x$ Catalysts Based on $Mn_xCo_{3-x}O_4$ Nanocages Derived from Metal−Organic Frameworks

Lei Zhang, Liyi Shi, Lei Huang, Jianping Zhang, Ruihua Gao, and Dengsong Zhang*

Research Center of Nano Science and Technology, Shanghai University, 99 Shangda Road, Shanghai 200444, China

Supporting Information

ABSTRACT: Herein, we have rationally designed and originally developed a high-performance deNO$_x$ catalyst based on hollow porous $Mn_xCo_{3-x}O_4$ nanocages with a spinel structure thermally derived from nanocube-like metal−organic frameworks ($Mn_3[Co(CN)_6]_2{\cdot}nH_2O$), which are synthesized via a self-assemble method. The as-prepared catalysts have been characterized systematically to elucidate their morphological structure and surface properties. As compared with conventional $Mn_xCo_{3-x}O_4$ nanoparticles, $Mn_xCo_{3-x}O_4$ nanocages possess a much better catalytic activity at low-temperature regions, higher N_2 selectivity, more extensive operating-temperature window, higher stability, and SO_2 tolerance. The feature of hollow and porous structures provides a larger surface area and more active sites to adsorb and activate reaction gases, resulting in the high catalytic activity. Moreover, the uniform distribution and strong interaction of manganese and cobalt oxide species not only enhance the catalytic cycle but also inhibit the formation of manganese sulfate, resulting in high catalytic cycle stability and good SO_2 tolerance. In light of the various characterization results, the excellent deNO$_x$ performance of $Mn_xCo_{3-x}O_4$ nanocages can be attributed to the hollow and porous structures, the uniform distribution of active sites, as well as the strong interaction of manganese and cobalt oxide species. The excellent catalytic performance suggests that $Mn_xCo_{3-x}O_4$ nanocages are promising candidates for low-temperature deNO$_x$ catalysts. More importantly, the present study indicates that the hollow porous architectures and well-dispersed active components can effectively enhance the performance of catalysts.

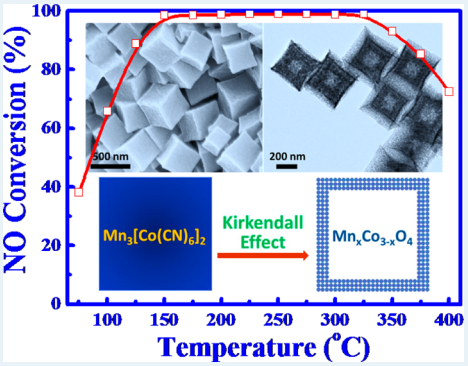

KEYWORDS: *DeNO$_x$ catalysts, SCR, hierarchically, nanocage, MOFs*

INTRODUCTION

Nitrogen oxides (NO_x) emitting from combustion of fossil fuels are currently considered as the dominant sources of atmospheric pollution, which has given rise to a variety of health-related and environmental issues, such as photochemical smog, acid rain, ozone depletion, and greenhouse effects.[1−5] The selective catalytic reduction (SCR) of NO with NH_3 is nowadays well-established as the most promising technology to eliminate NO_x.[6−8] Vanadium-based catalysts are used worldwide due to the desirable catalytic activity typically at 300−400 °C.[9,10] However, some inevitable drawbacks of this class of catalysts are still present, such as the toxicity of VO_x, narrow operation temperature window, and especially the poor activity at low-temperature regions.[11,12] It is hence extremely desirable to develop robust deNO$_x$ catalysts with low-temperature activity.[13,14]

On the basis of the good low-temperature activity and inherent environmentally benign characters, Mn-based catalysts have been widely developed for SCR of NO with NH_3 recently.[15−20] Unfortunately, Mn-based catalysts are very sensitive to the presence of SO_2 in the exhaust, which can induce a severe deactivation.[21,22] Recently, it has been reported that the SO_2 tolerance and catalytic activity of Mn-based catalysts could be enhanced by introducing the other transition metal oxides.[23,24] Qi et al. demonstrated that SO_2 resistance of MnO_x has been highly improved by CeO_2 due to the interaction of MnO_x and CeO_2.[24] Chen et al. found that the SO_2 tolerance and catalytic activity of MnO_x have been effectively enhanced by chromium oxide due to the formation of $CrMn_{1.5}O_4$ phase.[22] Yang et al. have studied the NH_3−SCR of NO over Mn−Fe spinel oxides, and they found that the catalysts deactivated by SO_2 could be regenerated after the water washing treatment.[23] Despite the progress achieved to date, it is still a challenge to develop low-temperature Mn-based deNO$_x$ catalysts with a high SO_2 tolerance and stability.

Co-based oxides have long been explored extensively in catalysis, due to advantageous morphology characteristics and unique redox properties.[25−29] Previous studies have already reported that the coupling of Mn and Co species has dramatically enhanced the redox properties of $Mn_xCo_{3-x}O_4$, which exhibits much better catalytic activity for the removal of formaldehyde as compared with MnO_x and Co_3O_4, attributed to the interaction of the Mn and Co species and generation of abundant reactive oxygen species.[30−32] However, it should be noted that $Mn_xCo_{3-x}O_4$ was generally prepared by the coprecipitation method, and thus it is difficult to achieve the

Received: December 12, 2013
Revised: April 17, 2014
Published: April 22, 2014

   dx.doi.org/10.1021/cs401185c | ACS Catal. 2014, 4, 1753−1763

Scheme 1. Schematic Illustration of the Formation of Hollow $Mn_xCo_{3-x}O_4$ Nanocages Derived from $Mn_3[Co(CN)_6]_2{\cdot}nH_2O$ Precursor Nanocubes

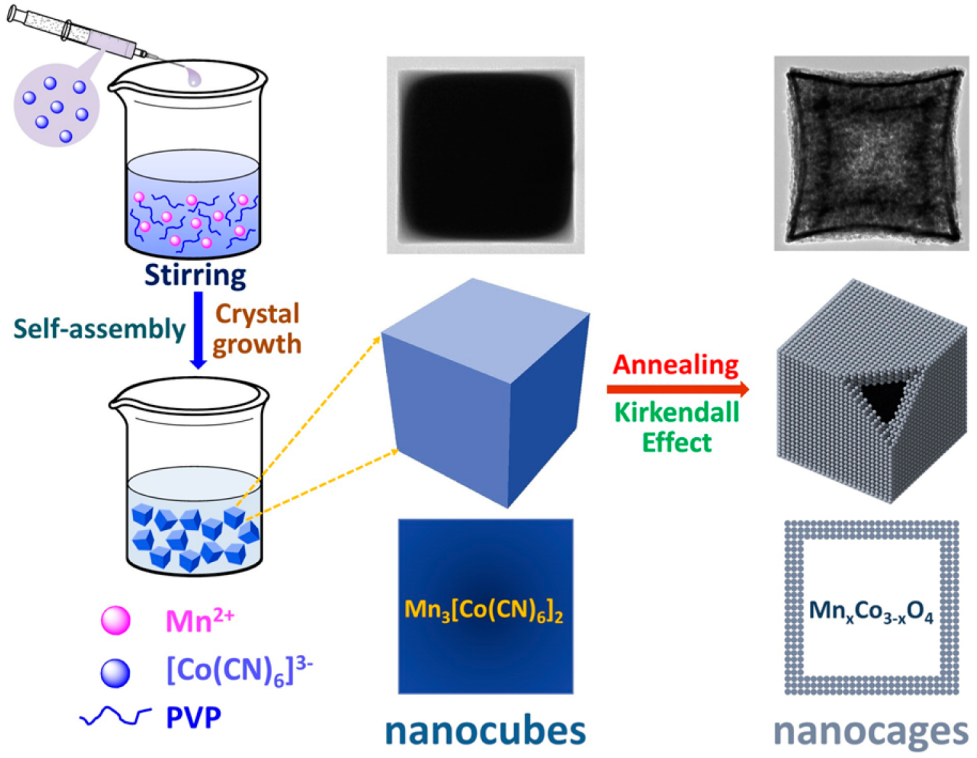

high dispersion of active components required for high performance catalysts, due to the difference for the solubility product constant (K_{sp}) of manganese and cobalt hydroxides. Moreover, due to the high surface energies, the traditional $Mn_xCo_{3-x}O_4$ nanoparticles could agglomerate easily during the catalytic process, resulting in the decline of catalytic activity. Accordingly, so far, little has been reported on $Mn_xCo_{3-x}O_4$ for SCR of NO with NH_3.

In addition to the desirable compositions, previous studies have already demonstrated that the catalytic behaviors of catalysts are also strongly dependent on the morphology and hierarchical structure of the materials.[33,34] In particular, the hierarchically porous structure with a uniform porous texture and hollow structures would greatly benefit the performance of catalysts, due to offering a high specific surface area, short diffusion length of reaction gases, and efficient channels for mass transport.[35,36] Therefore, the rational design and controllable synthesis of $Mn_xCo_{3-x}O_4$ with uniform compositions and hierarchically porous structures are highly desirable for the enhancement of its catalytic performance but still remain as significant challenges.

Prussian blue analogues (PBAs) are a class of crystalline metal−organic frameworks (MOFs) constructed from divalent and trivalent metal ions bridged by cyanide ligands and can be made with uniform composition and size, as well as diverse morphologies and architectures.[37] As a result of the unique reactivity and special thermal properties, the MOFs could be applied as precursors to synthesize hierarchical materials with the hollow and/or porous structures.[38−40] Herein, starting with shape-controlled synthesis of $Mn_3[Co(CN)_6]_2{\cdot}nH_2O$ nanocubes as precursors, we rationally designed and originally developed a high-performance deNO_x catalyst based on $Mn_xCo_{3-x}O_4$ nanocages with hollow and porous structures derived from $Mn_3[Co(CN)_6]_2{\cdot}nH_2O$ nanocubes via an annealing treatment in air. As illustrated in Scheme 1, the fabrication process of $Mn_xCo_{3-x}O_4$ nanocages with hollow and porous structures involves two steps. The first step involved the shape-controlled synthesis of $Mn_3[Co(CN)_6]_2{\cdot}nH_2O$ precursor nanocubes with a well-defined crystal structure. In this step, polyvinylpyrrolidone (PVP) is employed as an effective capping agent to direct the anisotropic growth of metal cyanide coordination polymer through preferential adsorption on specific crystal facets. This preferential capping effect of PVP can drive the Mn^{2+} and $[Co(CN)_6]^{3-}$ to self-assemble into nanocrystals with a cubic shape. After an Ostwald ripening process, the size of nanocrystals increases and homogenizes. Simultaneously, the crystallinity of $Mn_3[Co(CN)_6]_2{\cdot}nH_2O$ precursor nanocubes is further enhanced, and the structural defects decrease. In the second step, $Mn_xCo_{3-x}O_4$ nanocages with hollow and porous structures are formed by annealing $Mn_3[Co(CN)_6]_2{\cdot}nH_2O$ precursor nanocubes based on the Kirkendall effect. A variety of organic and inorganic species in the as-prepared $Mn_3[Co(CN)_6]_2{\cdot}nH_2O$ precursor nanocubes, including PVP, crystal water, and cyanide ligand can be decomposed and volatilized by an annealing treatment in air to generate the hollow and porous structures. The as-prepared catalysts were characterized systematically, and their NH_3−SCR activity, stability, and SO_2 tolerance were also investigated. As compared with $Mn_xCo_{3-x}O_4$ nanoparticles, $Mn_xCo_{3-x}O_4$ nanocages demonstrated a much better NH_3−SCR activity, higher N_2 selectivity, more extensive operating-temperature window, higher stability, and SO_2 tolerance.

EXPERIMENT SECTION

Catalyst Preparation. All the chemicals were of analytical grade and used without further purification. The $Mn_3[Co-$

dx.doi.org/10.1021/cs401185c | ACS Catal. 2014, 4, 1753−1763

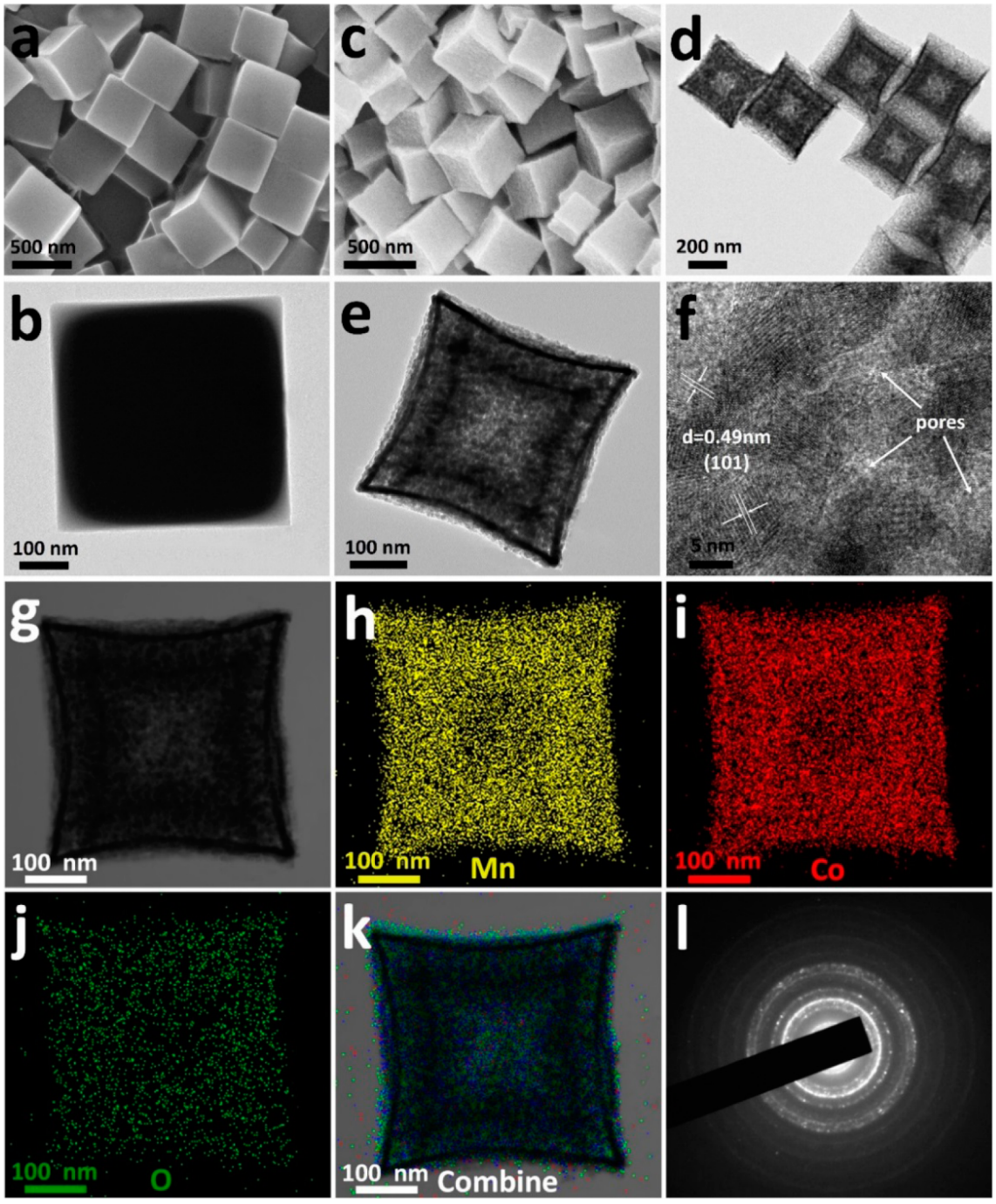

Figure 1. SEM (a) and TEM (b) images of $Mn_3[Co(CN)_6]_2{\cdot}nH_2O$ precursor nanocubes; SEM (c), TEM (d and e) and HRTEM (f) images, BF-STEM (g) image, EDX-mapping (h–k) images, and the corresponding SAED (l) pattern of $Mn_xCo_{3-x}O_4$ nanocages derived from $Mn_3[Co(CN)_6]_2{\cdot}nH_2O$ precursor nanocubes by annealing in air.

$(CN)_6]_2{\cdot}nH_2O$ precursor nanocubes were synthesized with the modified self-assemble methods.[41] In a typical synthesis process, 1.5 g of polyvinylpyrrolidone (PVP, K-30) and 0.22 g of $Mn(CH_3COO)_2{\cdot}4H_2O$ were first dissolved into 90 mL of mixed aqueous solution with deionized water and ethanol (v/v = 1:2) under magnetic stirring to form a transparent solution. Subsequently, 60 mL of an aqueous solution of $K_3Co(CN)_6$ (0.16 g) was added dropwise into the above solution under magnetic stirring. Then, the mixed solution was maintained under ambient conditions. After aging for 24 h, the white precipitate, which was $Mn_3[Co(CN)_6]_2{\cdot}nH_2O$ nanocubes, was collected by filtration, washed by deionized water and absolute ethanol several times, and finally dried at room temperature for 12 h. In order to obtain the porous $Mn_xCo_{3-x}O_4$ nanocages, the as-synthesized $Mn_3[Co(CN)_6]_2{\cdot}nH_2O$ precursor nanocubes were annealed in air at 450 °C for 2 h with a slow heating rate of 1 °C·min^{-1}. Thanks to such a slow heating rate, the porous $Mn_xCo_{3-x}O_4$ nanocages can withstand the annealing process and retain the well-defined morphology.

For comparison, the conventional $Mn_xCo_{3-x}O_4$ nanoparticles were prepared according to literature with some modifica-

dx.doi.org/10.1021/cs401185c | ACS Catal. 2014, 4, 1753–1763

tions.[42] The detailed procedure could be found in Supporting Information.

Characterization. The morphology and structure of the catalysts were characterized by scanning electron microscopy (SEM, JEOL JEM-200CX), transmission electron microscopy (TEM, JEOL JEM-200CX), and high-resolution TEM (HRTEM, JEOL JEM-2100F). Energy-dispersive X-ray (EDX) analysis and elemental mapping were performed to obtain the component of the samples using an Inca Energy 200 TEM system from Oxford Instruments. X-ray diffraction (XRD) patterns were performed with a Rigaku D/MAS-RB X-ray diffractometer employing Cu Kα (40 kV, 40 mA) radiation. Thermogravimetric analysis (TGA, SHIMADZU DTG-60H) was used to investigate the thermal decomposition behavior of the samples. The temperature was increased from room temperature to 800 °C at a rate of 10 °C·min^{-1}. N_2 adsorption−desorption isotherms were obtained at 77 K using an ASAP 2020 M Micromeritics. Prior to N_2 adsorption, the samples were degassed at 300 °C for 4 h. The specific surface areas were determined using the Brunauer−Emmett−Teller (BET) equation. The pore volumes, average pore diameters, and pore size distributions were determined by the Barrett−Joyner−Halenda (BJH) method from the desorption branches of the isotherms. X-ray photoelectron spectroscopy (XPS) experiments were performed on a RBD upgraded PHI-5000C ESCA system with Mg Kα radiation. The whole spectra (0−1100 (1200) eV) and the narrow spectra of all the elements with much high resolution were both recorded by using RBD 147 interface (RBD Enterprises, U.S.A.) through the AugerScan 3.21 software. Binding energies were calibrated by using the containment carbon (C1s = 284.6 eV). H_2 temperature-programmed reduction (H_2-TPR) was performed on a Tianjin XQ TP5080 autoadsorption apparatus. Prior to H_2-TPR experiment, 50 mg of catalysts was pretreated with N_2 with a total flow rate of 30 mL·min^{-1} at 300 °C for 0.5 h, then cooled down to room temperature in the N_2 atmosphere. Finally, the reactor temperature was raised to 600 °C at a constant heating rate of 10 °C·min^{-1} in a flow of H_2 (5 vol %)/N_2 (30 mL·min^{-1}). The H_2 consumption during the experiment was monitored by a TCD. NH_3 temperature-programmed desorption (NH_3-TPD) was performed on the same Tianjin XQ TP5080 autoadsorption apparatus. Prior to the NH_3-TPD experiments, the catalysts (150 mg) were pretreated at 300 °C in a flow of N_2 (30 mL·min^{-1}) for 0.5 h and cooled to 100 °C under N_2 flow. Then the samples were exposed to a flow of NH_3 at 100 °C for 1 h, followed by N_2 purging for 0.5 h. Finally, the reactor temperature was raised to 800 °C in the N_2 flow at a constant rate of 10 °C·min^{-1}. In situ diffuse reflectance infrared Fourier transform spectroscopy (in situ DRIFTS) experiments were performed on an FTIR spectrometer (Nicolet 6700) equipped with a Harrick DRIFT cell and an MCT/A detector. Prior to each experiment, the catalysts were pretreated at 350 °C in a flow of N_2 (50 mL·min^{-1}) for 0.5 h and cooled to target temperature under N_2 flow. Background spectra were recorded in the N_2 flow and automatically subtracted from the corresponding spectra. All the DRIFTS spectra were collected by accumulating 64 scans at a 4 cm^{-1} resolution.

Catalytic Performance Tests. The NH_3−SCR activity tests were performed in a fixed-bed quartz reactor with an inner diameter of 8 mm under the following typical reaction condition: [NO] = [NH_3] = 500 ppm, [O_2] = 3 vol %, [H_2O] = 8 vol % (when used), [SO_2] = 200 ppm (when used), N_2 balance. For each SCR activity test, 0.4 g of catalysts (crushed and sieved to 40−60 mesh) was used . The total flow rate of feed gases was 210 mL min^{-1}, and thus a gas hourly space velocity (GHSV) of 38 000 h^{-1} was obtained. The concentration of the feed gases and the effluent streams were analyzed continuously by a KM9106 flue gas analyzer. The concentrations of N_2O and NH_3 were measured by a Transmitter IR N_2O analyzer and an IQ350 ammonia analyzer. All data were recorded at the chosen temperature from 75 to 400 °C, after the reaction reached a steady state. NO conversion was calculated according to the following equation:

$$\text{NO conversion } (\%) = \frac{[\text{NO}]_{\text{in}} - [\text{NO}]_{\text{out}}}{[\text{NO}]_{\text{in}}} 100\%$$

where the $[NO]_{in}$ and $[NO]_{out}$ indicated the inlet and outlet concentration at steady-state, respectively.

RESULTS AND DISCUSSION

Characteristics of the Catalysts. The morphology and structure of the $Mn_3[Co(CN)_6]_2{\cdot}nH_2O$ precursor nanocubes were investigated by SEM and TEM. The SEM image of the as-prepared $Mn_3[Co(CN)_6]_2{\cdot}nH_2O$ precursor nanocubes (Figure 1a) clearly exhibits that these nanocubes have well-defined shapes and smooth facets, indicating the single-crystal-like feature of the $Mn_3[Co(CN)_6]_2{\cdot}nH_2O$ nanocubes. A panoramic SEM image (Figure S1a, Supporting Information) reveals that these nanocubes possess a highly morphological uniformity with an average particle size of 468 nm (Figure S1b, Supporting Information). The typical TEM images (Figure 1b and Figure S1c, Supporting Information) clearly indicate that each nanocube possesses well-defined crystal structures with hardly any defects and discernible porosity. Furthermore, the selected-area electron diffraction (SAED) pattern (Figure S1d, Supporting Information) also evidently confirms the single-crystal character of the $Mn_3[Co(CN)_6]_2{\cdot}nH_2O$ precursor nanocubes, suggesting the uniform arrangement of Mn and Co atoms in $Mn_3[Co(CN)_6]_2{\cdot}nH_2O$ precursor nanocubes, which agrees well with the previous reports.[40] The crystallographic structure, chemical composition and phase purity of the $Mn_3[Co(CN)_6]_2{\cdot}nH_2O$ precursor nanocubes was determined by the XRD. All of the diffraction peaks in the XRD pattern (Figure S2, Supporting Information) is highly consistent with the characteristic reflections of face-center-cubic $Mn_3[Co(CN)_6]_2{\cdot}nH_2O$ with an *Fm*3*m* system (JCPDS card no. 51-1898). Moreover, only the sharp and strong characteristic diffraction peaks of $Mn_3[Co(CN)_6]_2{\cdot}nH_2O$ precursor nanocubes have been detected, which suggests that the product possesses a high purity and crystallinity.

The as-prepared $Mn_3[Co(CN)_6]_2{\cdot}nH_2O$ precursor nanocubes are not thermally stable, and they can be decomposed and transformed into the corresponding metal oxide by calcining in air. The TGA was performed to investigate the thermal behavior of $Mn_3[Co(CN)_6]_2{\cdot}nH_2O$ precursor nanocubes and guide the calcination process. As shown in the TGA curve (Figure S3, Supporting Information), the decomposition process of $Mn_3[Co(CN)_6]_2{\cdot}nH_2O$ precursor nanocubes possesses two distinct weight-loss steps attributed to the evaporation of crystal water (25−200 °C) and the oxidation of $Mn_3[Co(CN)_6]_2$ (300−400 °C), respectively.[43] According to the TGA curve, the $Mn_3[Co(CN)_6]_2{\cdot}nH_2O$ precursor nanocubes was annealed to convert into $Mn_xCo_{3-x}O_4$ at 450 °C for 2 h. Obviously, the overall cubic morphology of the

dx.doi.org/10.1021/cs401185c | ACS Catal. 2014, 4, 1753−1763

obtained $Mn_xCo_{3-x}O_4$ nanocages (Figure S4, Supporting Information) is well-preserved after annealing in air, benefiting from a slow heating rate. As revealed in Figure 1c, a magnified SEM image of $Mn_xCo_{3-x}O_4$ nanocages, the rough surface with some pores is observed. The hollow interior and detailed geometrical structure of the as-prepared $Mn_xCo_{3-x}O_4$ nanocages are directly elucidated by TEM and HRTEM images in Figure 1d–f. The sharp contrast between the inner center and outer edges indicates the formation of hollow structure. Meanwhile, it clearly shows that the $Mn_xCo_{3-x}O_4$ nanocages with uniform mesoporous shells are composed of small nanoparticles. In addition, the HRTEM image (Figure 1f) shows a distinct lattice fringe with an interplanar spacing of 0.49 nm, which matches well with the spacing between the (101) planes of the Mn–Co spinel phase.[40] The elemental mapping was performed to illustrate the spatial distribution of Mn and Co species in the $Mn_xCo_{3-x}O_4$ nanocage (Figure 1g). As revealed in Figure 1h–k, the elemental mapping results confirm the uniform distribution of Mn and Co species within the $Mn_xCo_{3-x}O_4$ nanocage, profiting from the uniform arrangement of Mn and Co atoms in $Mn_3[Co(CN)_6]_2{\cdot}nH_2O$ precursor nanocube. It is generally accepted that the good dispersion of active components is very important for its catalytic activity. The corresponding selected-area electron diffraction (SAED) patterns (Figure 1l) reveals the polycrystallinity of $Mn_xCo_{3-x}O_4$ nanocages. Figure 2 illustrates the

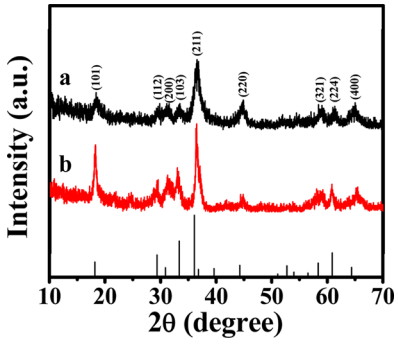

Figure 2. XRD patterns of the catalysts: (a) $Mn_xCo_{3-x}O_4$ nanocages and (b) $Mn_xCo_{3-x}O_4$ nanoparticles.

XRD patterns of $Mn_xCo_{3-x}O_4$ nanocages and nanoparticles. For both samples, all of the reflections could be assigned to the tetragonal spinel structure $Mn_xCo_{3-x}O_4$ with an *I*41/*amd* system (JCPDS card no. 77-0471). The diffraction peaks of $Mn_xCo_{3-x}O_4$ nanocages are weaker and broader than those of $Mn_xCo_{3-x}O_4$ nanoparticles, indicating a low crystallinity of $Mn_xCo_{3-x}O_4$ nanocages, which is in good agreement with the TEM analysis (Figure 1d and Figure S5, Supporting Information).

The N_2 adsorption–desorption was performed to characterize the texture and porosity of the catalysts. As illustrated in Figure 3, the N_2 adsorption–desorption isotherm of $Mn_xCo_{3-x}O_4$ nanocages reveals a typical type IV curve with two distinct hysteresis loops, indicating the presence of mesopores according to the definition of IUPAC. The double hysteresis loops indicate the porosity with different pore size. The hysteresis loop observed at low relative pressure (between 0.4 and 0.7) is type H2, which can be ascribed to the mesoporous walls of nanocages. The other one at higher relative pressure (between 0.75 and 1.0) could be correlated to the internal cavities of nanocages. Those results correspond

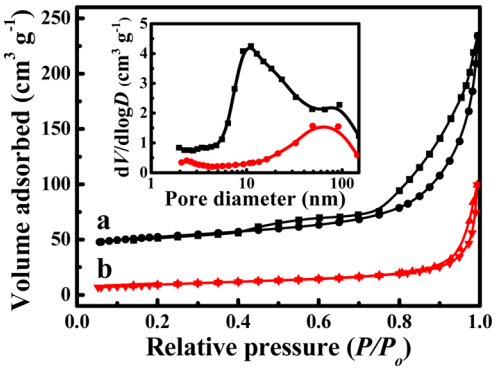

Figure 3. N_2 adsorption–desorption isotherms and corresponding size distribution curves (inset) of the catalysts: (a) $Mn_xCo_{3-x}O_4$ nanocages and (b) $Mn_xCo_{3-x}O_4$ nanoparticles.

closely to the TEM analyses. For $Mn_xCo_{3-x}O_4$ nanoparticles, the isotherm also shows a type IV curve with type H3 hysteresis loops, revealing the mesoporous features, which could be resulted from the packing of nanoparticles. As illustrated in the inset of Figure 3, the pore distribution of $Mn_xCo_{3-x}O_4$ nanocages shows a bimodal pore size distribution around 11 and 89 nm, which is in good conformity to the discussion above. By calculating the N_2 adsorption–desorption isotherms, the BET surface area of $Mn_xCo_{3-x}O_4$ nanocages is determined to be 77.1 $m^2{\cdot}g^{-1}$, which is much higher than that of $Mn_xCo_{3-x}O_4$ nanoparticles (33.1 $m^2{\cdot}g^{-1}$). Moreover, $Mn_xCo_{3-x}O_4$ nanocages present a great larger pore volume (0.318 $cm^3{\cdot}g^{-1}$) than that of $Mn_xCo_{3-x}O_4$ nanoparticles (0.156 $cm^3{\cdot}g^{-1}$), which results from their specific hollow and porous structures. The larger specific surface area and characteristic of hollow and porous structures of $Mn_xCo_{3-x}O_4$ nanocages are beneficial to the exposure of more active sites and adsorption of reactants, resulting in the latter excellent catalytic performance of $Mn_xCo_{3-x}O_4$ nanocages.

The information on the atomic concentrations and element chemical state on the catalysts surface were investigated by XPS measurements. Figure 4A–C illustrate the obtained XPS spectra of Mn 2p, Co 2p, and O 1s, respectively, and the corresponding surface atomic concentrations and the relative concentration ratios of different oxidation states are summarized in Table 1. As shown in Figure 4A, the Mn $2p_{3/2}$ spectra can be divided into three characteristic peaks attributed to Mn^{2+} (640.4 eV), Mn^{3+} (642.0 eV), and Mn^{4+} (644.1 eV), respectively, by performing peak-fitting deconvolutions.[14,22] From Table 1, it can be seen that the molar concentration of Mn on the surface of $Mn_xCo_{3-x}O_4$ nanocages (23.8%) is slightly higher than that of $Mn_xCo_{3-x}O_4$ nanoparticles (23.5%). It is noted that the relative surface content of Mn^{4+} (Mn^{4+}/Mn) over $Mn_xCo_{3-x}O_4$ nanocages (41.2%) is much higher than that of $Mn_xCo_{3-x}O_4$ nanoparticles (33.7%). It is clear that much more Mn^{4+} species are exposed on the surface of $Mn_xCo_{3-x}O_4$ nanocages. It has been demonstrated that the Mn^{4+} species and their redox cycle might be beneficial for the high activity in the NH_3–SCR reaction at low temperatures, attributed to the enhancement of NO oxidation to NO_2.[14,20,44,45]

The Co 2p XPS spectra (Figure 4B) exhibit two distinct peaks centered at 795.7 and 780.5 eV ascribed to Co $2p_{1/2}$ and Co $2p_{3/2}$ spin–orbital peaks, respectively.[28] The spin–orbit splitting is 15.2 eV, which is revealed the coexistence of Co^{2+} and Co^{3+} species.[28,46] The Co $2p_{3/2}$ spectra of the two catalysts are fitted into two peaks assigned to Co^{3+} (779.9 eV) and Co^{2+}

dx.doi.org/10.1021/cs401185c | ACS Catal. 2014, 4, 1753–1763

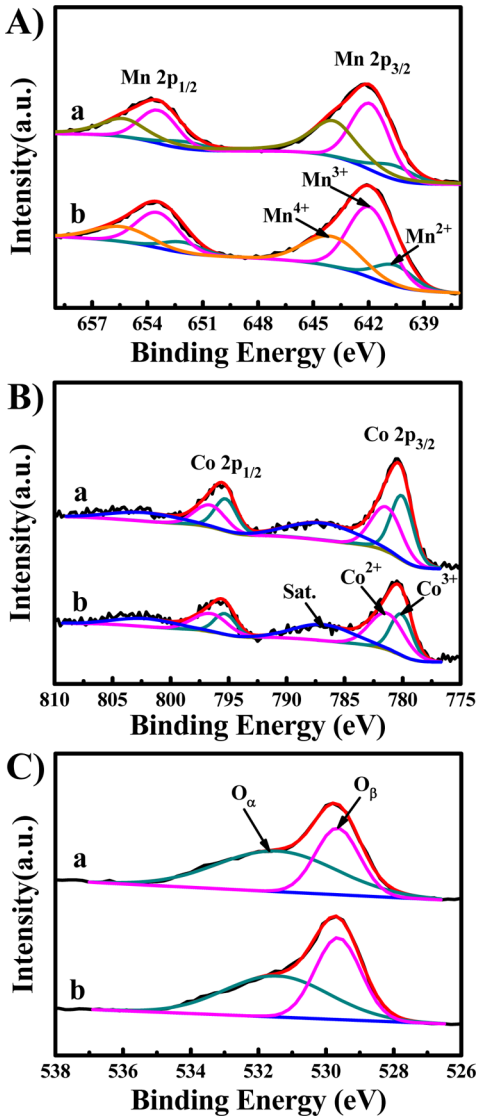

Figure 4. XPS spectra for Mn 2p (A), Co 2p (B), and O 1s (C) of the catalysts: (a) $Mn_xCo_{3-x}O_4$ nanocages and (b) $Mn_xCo_{3-x}O_4$ nanoparticles.

(781.5 eV), respectively.[28] The surface molar concentration of Co and the relative surface contents of Co^{3+} (Co^{3+}/Co) are also listed in Table 1. It is interesting that the Co and Co^{3+}/Co values for $Mn_xCo_{3-x}O_4$ nanocages are both higher than those for $Mn_xCo_{3-x}O_4$ nanoparticles. It is generally recognized that the more Co^{3+} species are preferable for redox properties over the Co-based catalysts, resulting in an enhancement of catalytic activity.[28,47] Moreover, Meng et al. investigated the surface properties of cobalt oxide nanocrystals with different shapes and found that the abundant Co^{3+} species on the surface of Co_3O_4 nanorods are beneficial to NH_3 chemisorption.[27] On the basis of the above discussion, it is reasonable to infer that Co^{3+} species play a critical role in the enhancement of catalytic activity.

In the case of O 1s spectra (Figure 4C), the spectra of the catalysts are fitted into two peaks ascribed to the lattice oxygen species centered at 529.7 eV and the chemisorbed oxygen species (O_2^{2-} or O^- belonging to defect-oxide or hydroxyl-like group) around 531.5 eV, denoted as O_β and O_α, respectively.[45] According to the XPS analysis, the percentage of O_α species on the $Mn_xCo_{3-x}O_4$ nanocage surface are much higher than that of nanoparticles, which could be attributed to the abundant defects induced by smaller crystal particles. It has been demonstrated that O_α species are more active than O_β species, attributing to their higher mobility.[48] Moreover, the presence of NO_2 in the gas mixture is beneficial to the SCR reaction, resulting from the enhancement of the "fast SCR" reaction.[15,49,50] Therefore, the higher percentage of O_α species are beneficial to the NH_3–SCR of NO, resulting in the promotion of the oxidation of NO to NO_2 and the subsequent facilitation of the "fast SCR" reaction.[45,51] In addition, a larger amount of surface hydroxyl-like groups could act as Brønsted acid sites to enhance the chemisorption of NH_3.[52] On the basis of the XPS analysis, it can be concluded that the excellent catalytic activity of $Mn_xCo_{3-x}O_4$ nanocages could be attributed to the more easy reducibility of Mn^{4+} and Co^{3+}, higher content of active Mn^{4+} and Co^{3+} cationic species, as well as higher content of active surface oxygen species.

It is well-known that the redox property of catalysts is remarkably related to the catalytic cycle in NH_3–SCR of NO. The H_2-TPR measurements are applied to evaluate the reducibility of the catalysts, and the obtained H_2-TPR profiles are illustrated in Figure 5. Both of the H_2-TPR profiles of the

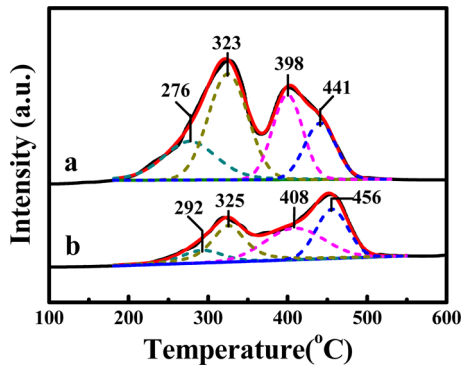

Figure 5. H_2-TPR profiles of the catalysts: (a) $Mn_xCo_{3-x}O_4$ nanocages and (b) $Mn_xCo_{3-x}O_4$ nanoparticles.

samples present two distinct H_2 consumption peaks. Previous studies have demonstrated that the H_2-TPR profile of Co_3O_4 presents two H_2 consumption peaks around 300 and 400 °C, ascribed to the stepwise reduction of $Co^{3+} \rightarrow Co^{2+} \rightarrow Co^0$.[47,53] It has also been reported that the profile of pristine MnO_x exhibits two reduction peaks at approximately 350 and 460 °C, belonging to the reduction of $Mn^{4+} \rightarrow Mn^{3+} \rightarrow Mn^{2+}$.[30,54] For $Mn_xCo_{3-x}O_4$ nanoparticles, the H_2-TPR profile presents two well-defined reduction peaks around 321 and 453 °C. By contrast, the second reduction peak of $Mn_xCo_{3-x}O_4$ nanocages

Table 1. Surface Atomic Concentrations of Mn, Co, O and the Relative Concentration Ratios

catalysts	Mn (%)	Co (%)	O (%)	Mn^{4+}/Mn (%)	Mn^{4+}/Mn^{3+}	Co^{3+}/Co (%)	Co^{3+}/Co^{2+}	O_α/O (%)	O_α/O_β
$Mn_xCo_{3-x}O_4$ nanocages	23.8	11.7	64.5	41.2	0.86	52.9	1.1	62.3	1.7
$Mn_xCo_{3-x}O_4$ nanoparticles	23.5	11.5	65.0	33.7	0.65	41.7	0.71	53.5	1.2

dx.doi.org/10.1021/cs401185c | ACS Catal. 2014, 4, 1753–1763

moves to low-temperature regions by about 52 °C, suggesting the better redox ability than that of $Mn_xCo_{3-x}O_4$ nanoparticles. The H_2 consumption (0.49 mmol) of $Mn_xCo_{3-x}O_4$ nanocages is quite close to the theoretical H_2 consumptions (0.47 mmol), which indicates that all of the Mn^{4+}, Mn^{3+}, and Co^{3+} in $Mn_xCo_{3-x}O_4$ nanocages has been reduced to Mn^{2+} and Co^0 below 500 °C. The excess H_2 consumption may be related to the abundant Mn^{4+}, Co^{3+}, and O_α species at the $Mn_xCo_{3-x}O_4$ nanocage surface, resulting from the larger specific surface area and hierarchical porous structure. However, for $Mn_xCo_{3-x}O_4$ nanoparticles, the H_2 consumption is 0.39 mmol, which suggests that a substantial fraction of Mn^{4+}, Mn^{3+}, and Co^{3+} has been reduced to Mn^{2+} and Co^0 below 500 °C. To clarify the detailed reduction processes, all reduction peaks were deconvoluted into four sub-bands and denoted as T_1, T_2, T_3, and T_4 from low to high temperature, attributed to the reduction processes of $Co^{3+} \rightarrow Co^{2+}$, $Mn^{4+} \rightarrow Mn^{3+}$, $Co^{2+} \rightarrow Co^0$, and $Mn^{3+} \rightarrow Mn^{2+}$, respectively. The corresponding sub-band areas are in good conformity to the XPS analysis of the catalysts. Moreover, the reduction peaks of Mn and Co oxide species for $Mn_xCo_{3-x}O_4$ shift to the low-temperature regions as compared to the pristine MnO_x and Co_3O_4 reported in the literature.[30,47,53,54] Thus, it is reasonable to deduce that there is a strong interaction between manganese oxide and cobalt oxide species in $Mn_xCo_{3-x}O_4$, especially for $Mn_xCo_{3-x}O_4$ nanocages. The presence of the strong interaction between manganese oxide and cobalt oxide species could play a synergistic role in the reducibility of the catalysts, leading to the enhancement of catalytic cycle in the NH_3−SCR of NO.

The chemisorption and activation of NH_3 on the surface acid sites of catalysts are generally viewed as the primary process in the NH_3−SCR of NO. The NH_3-TPD is performed to investigate the surface acid amount and strength of the catalysts, and the obtained NH_3-TPD profiles are shown in Figure 6. The NH_3-TPD profile of $Mn_xCo_{3-x}O_4$ nanocages

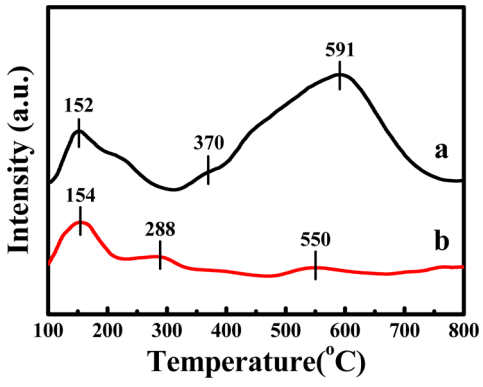

Figure 6. NH_3-TPD profiles of the catalysts: (a) $Mn_xCo_{3-x}O_4$ nanocages and (b) $Mn_xCo_{3-x}O_4$ nanoparticles.

exhibits three desorption peaks: the low-temperature desorption peak centered at 152 and 370 °C attributed to the NH_3 desorbed by weak acid sites and medium acid sites, and the very strong and broad peak observed at high temperature (591 °C) assigned to the strong acid sites on the catalysts. Whereas, in the case of $Mn_xCo_{3-x}O_4$ nanoparticles, three weaker NH_3 desorption peaks are observed at 154, 288, and 550 °C, respectively. Because the NH_3 molecules coordinated to the Lewis acid sites exhibit higher thermal stability than the NH_4^+ ions bound to the Brønsted acid sites, it can be deduced that the low-temperature peak is assigned to NH_4^+ ions bound to the Brønsted acid sites, and the desorption high-temperature peaks are associated with coordinated NH_3 molecular originating from the Lewis acid sites.[55] Moreover, it is well-known that the area and position of desorption peak are correlated with the acid amount and acid strength, respectively. As compared with $Mn_xCo_{3-x}O_4$ nanoparticles, the medium-high temperature desorption peaks of $Mn_xCo_{3-x}O_4$ nanocages obviously shift to the high-temperature region, which suggests that the strength of the Lewis acid sites on $Mn_xCo_{3-x}O_4$ nanocages is stronger than that of $Mn_xCo_{3-x}O_4$ nanoparticles. In addition, the NH_3-TPD profile of $Mn_xCo_{3-x}O_4$ nanocages reveals the much larger area, especially at the high-temperature region, indicating the presence of abundant Lewis acid sites. Therefore, $Mn_xCo_{3-x}O_4$ nanocages possess the stronger acid strength, which could be associated with the stronger interaction between manganese oxide and cobalt oxide species. More importantly, the higher number of Brønsted and Lewis acid sites could be attributed to its larger specific surface area and characteristic of the hollow and porous structures. The difference in the strength and number of acid sites on the two catalysts may result from their specific structural features, leading to the distinction of the catalytic performance.

The in situ DRIFTS experiments are performed to investigate the adsorption behaviors of the reactant molecules on the surface of the catalysts. The in situ DRIFTS of NH_3 adsorption over the two catalysts at various temperatures are shown in Figure 7a,b. The bands at 1129, 1196, and 1603 cm^{-1} can be assigned to the characteristic bands of NH_3 coordinated on Lewis acid sites,[45] and those at 1414, 1657, and 1683 cm^{-1} can be ascribed to the NH_4^+ bound to the Brønsted acid sites.[56−59] The bands at 1542 and 1558 cm^{-1} are assigned to the amide ($-NH_2$) species.[56,60,61] It is evident that the band intensity of Lewis acid (1129 and 1196 cm^{-1}) and Brønsted acid sites (1657 and 1683 cm^{-1}) over $Mn_xCo_{3-x}O_4$ nanocages are much higher than that over the $Mn_xCo_{3-x}O_4$ nanoparticle catalyst. These results suggest that $Mn_xCo_{3-x}O_4$ nanocages possess substantially more Lewis and Brønsted acid sites, which is in good agreement with the NH_3-TPD analysis. The in situ DRIFTS of NO + O_2 adsorption over the two catalysts at various temperatures are shown in Figure 7c,d. The bands at 1219 and 1250 cm^{-1} can be ascribed to the bridging nitrate,[51,56] and those at 1372 and 1450 cm^{-1} can be assigned to the M-NO_2 nitro compounds.[56,62,63] The band at 1324 cm^{-1} is assigned to *cis*-$N_2O_2^{2-}$,[60] and that at 1304 cm^{-1} is assigned to the bidentate nitrates.[64] The band at 1628 cm^{-1} can be assigned to the adsorbed NO_2 molecules.[57,60] With increasing temperature, the bands of bridging nitrate, *cis*-$N_2O_2^{2-}$, and adsorbed NO_2 species are gradually decreased. However, the band of M-NO_2 nitro species increases with the temperature rising (>150 °C). Remarkably, the intensities of bridging nitrate and adsorbed NO_2 species on $Mn_xCo_{3-x}O_4$ nanocages are much higher than those of nanoparticles at low-temperature regions (<150 °C). The above in situ DRIFTS analyses indicate the larger specific surface area and hierarchical porous structure have enhanced the chemisorption and activation of reactant molecules on $Mn_xCo_{3-x}O_4$ nanocages, resulting in the better low-temperature NH_3−SCR activity.

Catalytic Performance. The corresponding catalytic performance of $Mn_xCo_{3-x}O_4$ nanocages and nanoparticles, plotted as a function of temperature, are depicted in Figure 8. It is found that the $Mn_xCo_{3-x}O_4$ nanocages demonstrate a more extensive operating temperature window for NH_3−SCR of NO

dx.doi.org/10.1021/cs401185c | ACS Catal. 2014, 4, 1753−1763

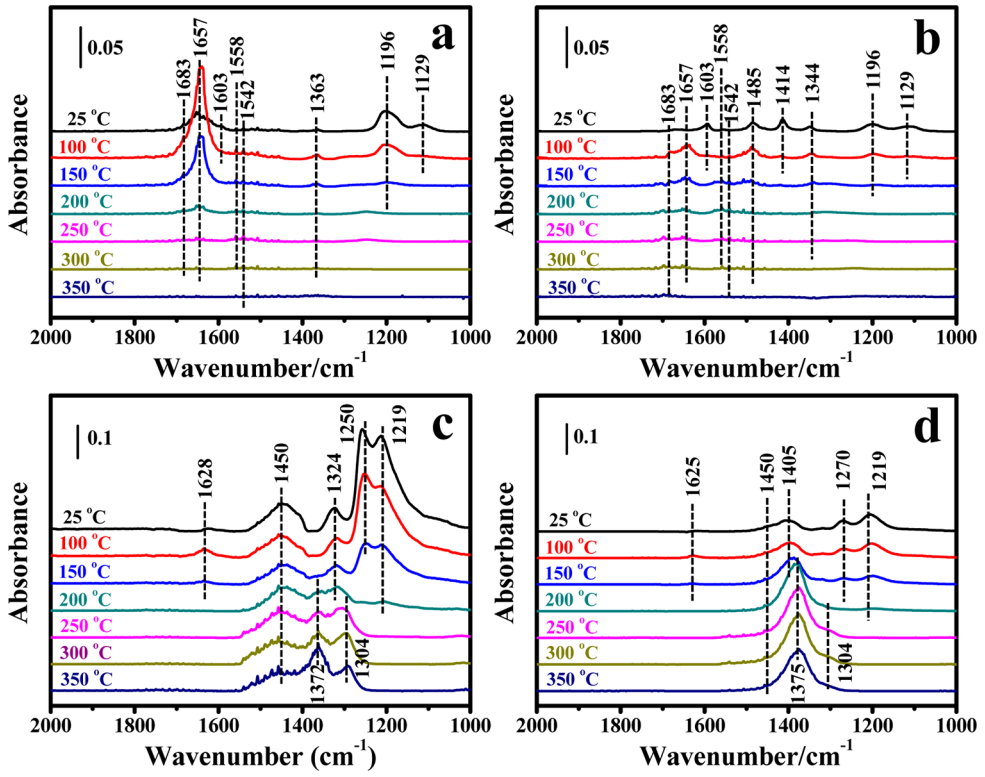

Figure 7. In situ DRIFTS of (a) NH_3 adsorption on $Mn_xCo_{3-x}O_4$ nanocages; (b) NH_3 adsorption on $Mn_xCo_{3-x}O_4$ nanoparticles; (c) NO + O_2 adsorption on $Mn_xCo_{3-x}O_4$ nanocages; (d) NO + O_2 adsorption on $Mn_xCo_{3-x}O_4$ nanoparticles from 25 to 350 °C.

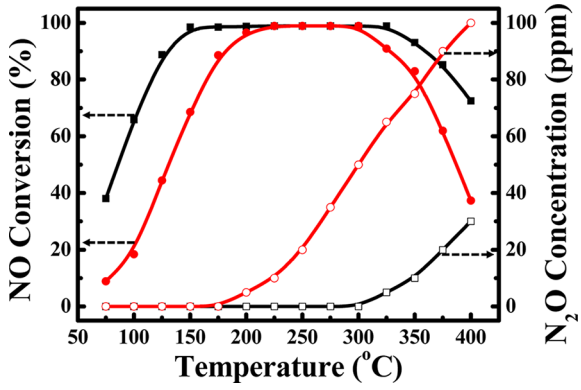

Figure 8. NH_3−SCR performance of the catalysts (square symbols: nanocages; circle symbols: nanoparticles). Reaction conditions: [NO] = [NH_3] = 500 ppm, [O_2] = 3 vol %, N_2 balance, and GHSV = 38 000 h^{-1}.

than $Mn_xCo_{3-x}O_4$ nanoparticles, under the identical operating conditions. It is remarkable to note that the $Mn_xCo_{3-x}O_4$ nanocages present a much better low-temperature activity than $Mn_xCo_{3-x}O_4$ nanoparticles. The light-off temperature of NO (T_{50}) of $Mn_xCo_{3-x}O_4$ nanocages is as low as 85 °C, and 98.5% NO conversion is achieved at 150 °C. The temperature window for 90% NO conversion ranges from 125 to 350 °C. By comparison, $Mn_xCo_{3-x}O_4$ nanoparticles achieve its T_{50} only above 130 °C, more than 45 °C higher than that of $Mn_xCo_{3-x}O_4$ nanocages. The excellent catalytic activity over $Mn_xCo_{3-x}O_4$ nanocages could be attributed to its characteristic of hollow and porous structures and the uniform distribution of active sites as well as the strong interaction of manganese and cobalt oxide species. The TEM and EDX-mapping images confirm the hollow porous structures of $Mn_xCo_{3-x}O_4$ nanocages and the uniform distribution of Mn and Co species within the $Mn_xCo_{3-x}O_4$ nanocages. The N_2 sorption results indicate that the $Mn_xCo_{3-x}O_4$ nanocages possess a larger specific surface area and pore volume, resulting in the generation of more available active sites, which could be in favor of the chemisorption of reactants. According to the XPS analysis, $Mn_xCo_{3-x}O_4$ nanocages have an abundance of Mn^{4+}, Co^{3+} cationic species and surface active oxygen species. The H_2-TPR analyses suggest that $Mn_xCo_{3-x}O_4$ nanocages possess much more reactive oxygen species and stronger interaction between manganese oxide and cobalt oxide species, resulting in its better reducibility, which could enhance catalytic cycle and lead to the excellent activity of the catalyst in the NH_3−SCR of NO. The NH_3-TPD results demonstrate that the $Mn_xCo_{3-x}O_4$ nanocages present not only the larger acid amount but also stronger acid strength, which could facilitate the chemisorption and activation of NH_3, resulting in the better performance in the NH_3−SCR of NO. To demonstrate the promotional effect of the interaction between manganese oxide and cobalt oxide species of $Mn_xCo_{3-x}O_4$ nanocages, the areal rates of the catalysts (i.e., the rates at 50 °C normalized by the BET surface area as defined in Supporting Information) are provided. The areal rate of $Mn_xCo_{3-x}O_4$ nanocages is 8.37×10^{-9} mol s^{-1} m^{-2}, much higher than that of nanoparticles (2.87×10^{-9} mol s^{-1} m^{-2}). This indicates that the strong interaction between manganese oxide and cobalt oxide species has remarkably enhanced the catalytic activity of $Mn_xCo_{3-x}O_4$ nanocages. Moreover, as compared to the other high-activity Mn-based catalysts reported previously, the $Mn_xCo_{3-x}O_4$ nanocages catalysts reveal better catalytic activity at similar reaction conditions (Table S1, Supporting Information).[23,24,60,65] Generally, N_2O is generated as byproduct due the nonselective oxidation of NH_3 in SCR of NO, which can greatly affect the

dx.doi.org/10.1021/cs401185c | ACS Catal. 2014, 4, 1753−1763

NH_3−SCR performance of the catalysts.[18] Thus, during NH_3−SCR of NO reaction over the catalysts, N_2O concentrations were also detected at various reaction temperatures in the range of 75 to 400 °C. As shown in Figure 8, the formation of N_2O over $Mn_xCo_{3-x}O_4$ nanoparticles was obviously detected, but the N_2O concentration was very low until 350 °C over $Mn_xCo_{3-x}O_4$ nanocages. To clarify the difference of the catalysts in N_2 selectivity, the NH_3 oxidation activities of two catalysts were investigated (Figure S6, Supporting Information). The NH_3 oxidation ability of $Mn_xCo_{3-x}O_4$ nanocages is obviously higher than that of nanoparticles, which indicates that $Mn_xCo_{3-x}O_4$ nanocages are more effective in NH_3 activation, benefiting from the hierarchically porous structures and the large BET surface area of $Mn_xCo_{3-x}O_4$ nanocages. These results are in good conformity to the NH_3-TPD analysis. However, the N_2O formation in NH_3 oxidation reaction over $Mn_xCo_{3-x}O_4$ nanocages is much lower than that over nanoparticles, suggesting that $Mn_xCo_{3-x}O_4$ nanocages are better in the inhibition of NH_3 unselective oxidation. These results indicate that $Mn_xCo_{3-x}O_4$ nanocages display much better N_2 selectivity than $Mn_xCo_{3-x}O_4$ nanoparticles, which is probably associated with the uniform distribution of active sites and synergistic role between manganese oxide and cobalt oxide species in the nanocages. As indicated by in situ DRIFTS analyses, the chemisorption and activation of reactant molecules on $Mn_xCo_{3-x}O_4$ nanocages are obviously enhanced, resulting in the improved low-temperature activity. Based on these favorable properties of the structure and component, the $Mn_xCo_{3-x}O_4$ nanocages exhibit excellent performance for the NH_3−SCR of NO.

Figure 9 illustrates the stability tests of the catalysts at 300 °C. During the test period, the NO conversion on $Mn_xCo_{3-x}O_4$ nanocages is maintained. As time elapses, in contrast, a slight decrease of the catalytic activity over $Mn_xCo_{3-x}O_4$ nanoparticles is observed. To clarify the outstanding performance of $Mn_xCo_{3-x}O_4$ nanocages during the stability test, the SEM and N_2 adsorption−desorption measurements of the catalysts after the stability test were performed. Significantly, the morphologies and structure of $Mn_xCo_{3-x}O_4$ nanocages are retained well after the stability test at 300 °C for 24 h (Figure S7a, Supporting Information). N_2 adsorption−desorption analyses of the catalyst after the stability test confirm that both the BET surface area (76.8 $m^2 \cdot g^{-1}$) and the pore distribution of $Mn_xCo_{3-x}O_4$ nanocages are almost the same as the fresh one (Figure S7b, Supporting Information). Thus, the observation evidently suggests that $Mn_xCo_{3-x}O_4$ nanocages present a good stability under the identical reaction conditions, which is attributed to the characteristic of hollow and porous structures as well as the strong interaction between manganese oxide and cobalt oxide species.

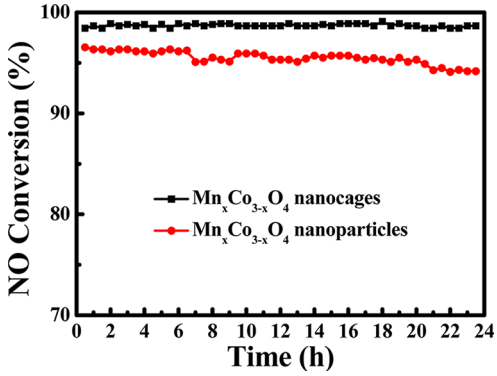

Figure 9. Stability test of the catalysts at 300 °C. Reaction conditions: [NO] = [NH_3] = 500 ppm, [O_2] = 3 vol %, N_2 balance, and GHSV = 38 000 h^{-1}.

Even after desulfurization, the residual H_2O (5−10 vol %) and SO_2 (100−200 ppm) in exhaust fumes can induce the poisoning and deactivation of catalysts.[66,67] Therefore, the impact of H_2O and SO_2 on the SCR activity of catalysts was investigated.

Figure 10a shows the H_2O resistance tests of the catalysts in the presence of 8 vol % H_2O at 175 °C. The NO conversion of $Mn_xCo_{3-x}O_4$ nanocages and nanoparticles is 99% and 89%, respectively, in the absence of H_2O. The addition of steam induces a slight decline of the NO conversion over both of the catalysts. However, after removing the water, the NO conversions on $Mn_xCo_{3-x}O_4$ nanocages and nanoparticles are both restored to their original level. It has been demonstrated that the inhibition of water caused by the competition between water and ammonia on the active sites is reversible.[14,67] These results indicate that both of the catalysts have a good capacity for water resistance.

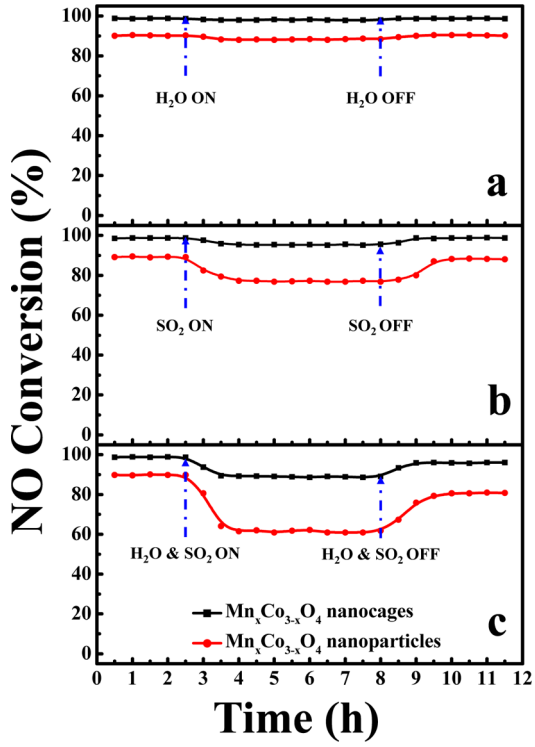

Figure 10. (a) H_2O resistance, (b) SO_2 tolerance, and (c) H_2O and SO_2 synergetic effect study of the catalysts at 175 °C. Reaction conditions: [NO] = [NH_3] = 500 ppm, [O_2] = 3 vol %, [H_2O] = 8 vol % (when used), [SO_2] = 200 ppm (when used), N_2 balance, and GHSV = 38 000 h^{-1}.

Figure 10b depicts the SO_2 tolerance tests of the catalysts in the presence of 200 ppm of SO_2 at 175 °C. The NO conversion over $Mn_xCo_{3-x}O_4$ nanocages decreases slightly after introducing 200 ppm of SO_2, and it then reaches a steady state. After switching SO_2 off, the activity gradually recovers to the initial value and remains unchanged. By contrast, in the case of $Mn_xCo_{3-x}O_4$ nanoparticles, the introduction of SO_2 induces a dramatic decrease from 89% to 77%. Interestingly, the NO

dx.doi.org/10.1021/cs401185c | ACS Catal. 2014, 4, 1753−1763

conversion over $Mn_xCo_{3-x}O_4$ nanoparticles is also restored to the initial value after eliminating SO_2. These results demonstrate that both of the catalysts are highly sulfur-resistant, and the inhibition of SO_2 is reversible. According to previous studies, it has been demonstrated that the deactivation of the catalysts caused by SO_2 are commonly attributed to the following two aspects.[18,67−69] First, ammonium sulfate species were generated and block the active sites of the catalyst surface, leading to a reversible deactivation. Second, active phases of the catalysts could be sulfated to form stable sulfate species, resulting in an irreversible deactivation. Chen et al. found that the SO_2 tolerance and catalytic activity of MnO_x have been effectively enhanced by chromium oxide due to the formation of the $CrMn_{1.5}O_4$ phase.[22] Similarly, Yang et al. have studied the NH_3−SCR of NO over Mn−Fe spinel, and they found that the catalysts deactivated by SO_2 could be regenerated after the water washing treatment.[23] Therefore, it is reasonable to deduce that the SO_2 resistance of Mn-based catalysts could be enhanced by cobalt species, which might be related to the stable spinel structure and the strong interaction between MnO_x and CoO_x species, leading to the inhibition of manganese sulfate formation on the catalyst surface. More importantly, Yu et al. have reported that mesoporous Mn-base catalysts prepared by a sol−gel method possess a good SO_2 resistance during a long-time (60 h) test of the SCR reactions in a SO_2-contaning gas, and they attributed the good SO_2 resistance of mesoporous Mn-based catalysts to the mesopore structure, which enables the formation and decomposition of ammonium sulfate to reach a dynamic balance in the SCR reaction, through comparing the TG, XPS, FTIR, and N_2 adsorption analysis of the catalysts prepared by the impregnation and sol−gel methods.[21] Huang et al. have studied the NH_3−SCR of NO over manganese supported on mesoporous silica and found similar results.[67] In short, for $Mn_xCo_{3-x}O_4$ nanocages, the better SO_2 tolerance may be ascribed to the hierarchically porous structure, larger number of active sites, and stronger interaction between MnO_x and CoO_x compared with $Mn_xCo_{3-x}O_4$ nanoparticles.

The combined impact of H_2O and SO_2 on SCR activity were also investigated (Figure 10c). The coexistence of H_2O and SO_2 induces a 10% decrease in the NO conversion over $Mn_xCo_{3-x}O_4$ nanocages, but the NO conversion is recovered to 96%, after cutting off the supply of H_2O and SO_2. However, the activity on $Mn_xCo_{3-x}O_4$ nanoparticles decreases sharply under the coexistence of H_2O and SO_2. Nevertheless, the removal of H_2O and SO_2 from the feed gas gradually raises the NO conversion on the $Mn_xCo_{3-x}O_4$ nanoparticles to 81%. The above results indicate that there is a synergistic inhibition effect between H_2O and SO_2 in the SCR reaction. Under the coexistence of H_2O and SO_2, the rapid formation of ammonium sulfate species and deposition on the catalyst surface block the active sites of the catalysts surface, resulting in reduction of the catalytic activity. It can be concluded from the above results that $Mn_xCo_{3-x}O_4$ nanocages are highly sulfur-tolerant and water-resistant, which is attributed to the hierarchically porous structures, the uniform distribution of active sites as well as the strong interaction of manganese and cobalt oxide species.

CONCLUSIONS

In summary, we have successfully fabricated porous $Mn_xCo_{3-x}O_4$ nanocages with a spinel structure as high-performance deNO_x catalysts, which are derived from $Mn_3[Co(CN)_6]_2{\cdot}nH_2O$ precursor nanocubes via a simple annealing process. The $Mn_xCo_{3-x}O_4$ nanocages display an enhanced NH_3−SCR activity, high N_2 selectivity, wide operating-temperature window, high stability, and improved SO_2 tolerance. It has been demonstrated that the characteristic of hollow and porous structures, the uniform distribution of active sites, as well as the strong interaction of manganese and cobalt oxide species attribute to the excellent catalytic performance of $Mn_xCo_{3-x}O_4$ nanocages in NH_3−SCR of NO. The feature of hollow and porous structures provides a larger surface area and more active sites to adsorb and activate reagents, resulting in the higher catalytic activity. Moreover, the uniform distribution and the strong interaction of manganese and cobalt oxide species not only enhance the catalytic cycle but also inhibit the formation of manganese sulfate, resulting in high catalytic cycle stability and improved SO_2 tolerance. We also anticipate that the simple and scalable synthesis approach in the present study can be extended to fabricate other promising mixed metal oxides with hollow and porous structures on the nanoscale for various applications.

ASSOCIATED CONTENT

Supporting Information

XRD patterns, SEM images, TEM images, SEAD pattern, and TGA curves of the samples are available in Supporting Information. This material is available free of charge via the Internet at http://pubs.acs.org.

AUTHOR INFORMATION

Corresponding Author

*E-mail: dszhang@shu.edu.cn. Fax: +86-21-66136079. Tel: +86-21-66136081.

Notes

The authors declare no competing financial interest.

ACKNOWLEDGMENTS

The authors acknowledge the support of the National Natural Science Foundation of China (no. 51108258); the Doctoral Fund of Ministry of Education of China (no. 20123108120018); the Science and Technology Commission of Shanghai Municipality (nos. 13NM1401200 and 11NM0502200), Dongguan Municipal Research Program for Colleges and Institutes (no. 201210825000535), and the Shanghai First-Class Discipline Construction in Colleges and Universities. The authors would like to thank Mr. S. X. Cai and Mr. H. Hu for help with the experiments. We thank Mr. W. J. Yu and Mr. Y. L. Chu from the Analysis and Test Center of SHU for help with the TEM and SEM measurements. We also thank Dr. K. Zhang from the Analysis and Test Center of NERCN for help with the HRTEM measurements.

REFERENCES

(1) Johnson, C.; Henshaw, J.; Mclnnes, G. *Nature* **1992**, *355*, 69−71.
(2) Barbara, J.; Pitts, F.; James, N. P. J. *Science* **1997**, *276*, 1045−1051.
(3) Kim, C. H.; Qi, G. S.; Dahlberg, K.; Li, W. *Science* **2010**, *327*, 1624−1627.
(4) Parks, J. E. *Science* **2010**, *327*, 1584−1585.
(5) Smirniotis, P. G.; Pena, D. A.; Uphade, B. S. *Angew. Chem., Int. Ed.* **2001**, *40*, 2479−2482.
(6) Krishnan, A. T.; Boehman, A. L. *Appl. Catal., B* **1998**, *18*, 189−198.
(7) Kompio, P. G. W. A.; Brückner, A.; Hipler, F.; Auer, G.; Löffler, E.; Grünert, W. *J. Catal.* **2012**, *286*, 237−247.

(8) Forzatti, P.; Nova, I.; Tronconi, E. *Angew. Chem.* **2009**, *121*, 8516−8518.
(9) Kristensen, S. B.; Kunov-Kruse, A. J.; Riisager, A.; Rasmussenb, S. B.; Fehrmann, R. *J. Catal.* **2011**, *284*, 60−67.
(10) Gao, R. H.; Zhang, D. S.; Liu, X. G.; Shi, L. Y.; Maitarad, P.; Li, H. R.; Zhang, J. P.; Cao, W. G. *Catal. Sci. Technol.* **2013**, *3*, 191−199.
(11) Balle, P.; Geiger, B.; Kureti, S. *Appl. Catal., B* **2009**, *85*, 109−119.
(12) Mou, X. L.; Zhang, B. S.; Li, Y.; Yao, L. D.; Wei, X. J.; Su, D. S.; Shen, W. J. *Angew. Chem., Int. Ed.* **2012**, *51*, 2989−2993.
(13) Li, H. R.; Zhang, D. S.; Maitarad, P.; Shi, L. Y.; Gao, R. H.; Zhang, J. P.; Cao, W. G. *Chem. Commun.* **2012**, *48*, 10645−10647.
(14) Zhang, D. S.; Zhang, L.; Shi, L. Y.; Fang, C.; Li, H. R.; Gao, R. H.; Huang, L.; Zhang, J. P. *Nanoscale* **2013**, *5*, 1127−1136.
(15) Wang, W. C.; McCool, G.; Kapur, N.; Yuan, G.; Shan, B.; Nguyen, M.; Graham, U. M.; Davis, B. H.; Jacobs, G.; Cho, K.; Hao, X. H. *Science* **2012**, *337*, 832−835.
(16) Peña, D. A.; Uphade, B. S.; Smirniotis, P. G. *J. Catal.* **2004**, *221*, 421−431.
(17) Zhang, D. S.; Zhang, L.; Fang, C.; Gao, R. H.; Qian, Y. L.; Shi, L. Y.; Zhang, J. P. *RSC Adv.* **2013**, *3*, 8811−8819.
(18) Park, E.; Kim, M.; Jung, H.; Chin, S.; Jurng, J. *ACS Catal.* **2013**, *3*, 1518−1525.
(19) Gao, R. H.; Zhang, D. S.; Maitarad, P.; Shi, L. Y.; Rungrotmongkol, T.; Li, H. R.; Zhang, J. P.; Cao, W. G. *J. Phys. Chem. C* **2013**, *117*, 10502−10511.
(20) Fang, C.; Zhang, D. S.; Cai, S. X.; Zhang, L.; Huang, L.; Li, H. R.; Maitarad, P.; Shi, L. Y.; Gao, R. H.; Zhang, J. P. *Nanoscale* **2013**, *5*, 9199−9207.
(21) Yu, J.; Guo, F.; Wang, Y. L.; Zhu, J. H.; Liu, Y. Y.; Su, F. B.; Gao, S. Q.; Xu, G. W. *Appl. Catal., B* **2010**, *95*, 160−168.
(22) Chen, Z. H.; Yang, Q.; Li, H.; Li, X. H.; Wang, L. F.; Tsang, S. C. *J. Catal.* **2010**, *276*, 56−65.
(23) Yang, S. J.; Wang, C. Z.; Li, J. H.; Yan, N. Q.; Ma, L.; Chang, H. Z. *Appl. Catal., B* **2011**, *110*, 71−80.
(24) Qi, G. S.; Yang, R. T. *J. Catal.* **2003**, *217*, 434−441.
(25) Choi, S. O.; Penninger, M.; Kim, C. H.; Schneider, W. F.; Thompson, L. T. *ACS Catal.* **2013**, *3*, 2719−2728.
(26) Wang, C. A.; Li, S.; An, L. N. *Chem. Commun.* **2013**, *49*, 7427−7429.
(27) Meng, B.; Zhao, Z. B.; Wang, X. Z.; Liang, J. J.; Qiu, J. S. *Appl. Catal., B* **2013**, *129*, 491−500.
(28) Zhu, Z. Z.; Lu, G. Z.; Zhang, Z. G.; Guo, Y.; Guo, Y. L.; Wang, Y. Q. *ACS Catal.* **2013**, *3*, 1154−1164.
(29) Xie, X. W.; Li, Y.; Liu, Z. Q.; Haruta, M.; Shen, W. J. *Nature* **2009**, *458*, 746−749.
(30) Aguilera, D. A.; Perez, A.; Molina, R.; Moreno, S. *Appl. Catal., B* **2011**, *104*, 144−150.
(31) Zhang, Q. H.; Liu, X. H.; Fan, W. Q.; Wang, Y. *Appl. Catal., B* **2011**, *102*, 207−214.
(32) Shi, C.; Wang, Y.; Zhu, A.; Chen, B.; Au, C. *Catal. Commun.* **2012**, *28*, 18−22.
(33) Zhou, K. B.; Li, Y. D. *Angew. Chem., Int. Ed.* **2012**, *51*, 602−613.
(34) Zhang, D. S.; Du, X. J.; Shi, L. Y.; Gao, R. H. *Dalton. Trans.* **2012**, *41*, 14455−14475.
(35) Parlett, C. M. A.; Wilson, K.; Lee, A. F. *Chem. Soc. Rev.* **2013**, *42*, 3876−3893.
(36) Lou, X. W.; Archer, L. A.; Yang, Z. C. *Adv. Mater.* **2008**, *20*, 3987−4019.
(37) Hu, M.; Belik, A. A.; Imura, M.; Yamauchi, Y. *J. Am. Chem. Soc.* **2013**, *135*, 384−391.
(38) Zhang, L.; Wu, H. B.; Madhavi, S.; Hng, H. H.; Lou, X. W. *J. Am. Chem. Soc.* **2012**, *134*, 17388−17391.
(39) Hu, L.; Yan, N.; Chen, Q. W.; Zhang, P.; Zhong, H.; Zheng, X. R.; Li, Y.; Hu, X. Y. *Chem.—Eur. J.* **2012**, *18*, 8971−8977.
(40) Hu, L.; Zhang, P.; Zhong, H.; Zheng, X. R.; Yan, N.; Chen, Q. W. *Chem.—Eur. J.* **2012**, *18*, 15049−15056.
(41) Hu, L.; Mei, J. Y.; Chen, Q. W.; Zhang, P.; Yan, N. *Nanoscale* **2011**, *3*, 4270−4274.
(42) Chen, Z. P.; Xing, J.; Jiang, H. B.; Yang, H. G. *Chem.—Eur. J.* **2013**, *19*, 4123−4127.
(43) Hu, L.; Zhang, P.; Chen, Q. W.; Zhong, H.; Hu, X. Y.; Zheng, X. R.; Wang, Y.; Yan, N. *Cryst. Growth Des.* **2012**, *12*, 2257−2264.
(44) Thirupathi, B.; Smirniotis, P. G. *J. Catal.* **2012**, *288*, 74−83.
(45) Liu, F. D.; He, H.; Ding, Y.; Zhang, C. B. *Appl. Catal., B* **2009**, *93*, 194−204.
(46) Bin, F.; Song, C. L.; Lv, G.; Song, J. O.; Cao, X. F.; Pang, H. T.; Wang, K. P. *J. Phys. Chem. C* **2012**, *116*, 26262−26274.
(47) Bai, B. Y.; Arandiyan, H.; Li, J. H. *Appl. Catal., B* **2013**, *142−143*, 677−683.
(48) Liu, F. D.; He, H. *J. Phys. Chem. C* **2010**, *114*, 16929−16936.
(49) Koebel, M.; Madia, G.; Raimondi, F.; Wokaun, A. *J. Catal.* **2002**, *209*, 159−165.
(50) Schwidder, M.; Heikens, S.; Detoni, A.; Geisler, S.; Berndt, M.; Bruckner, A.; Grunert, W. *J. Catal.* **2008**, *259*, 96−103.
(51) Shan, W. P.; Liu, F. D.; He, H.; Shi, X. Y.; Zhang, C. B. *Chem. Commun.* **2011**, *47*, 8046−8048.
(52) Zhang, L.; Zhang, D. S.; Zhang, J. P.; Cai, S. X.; Fang, C.; Huang, L.; Li, H. R.; Gao, R. H.; Shi, L. Y. *Nanoscale* **2013**, *5*, 9821−9829.
(53) Jiang, S. J.; Song, S. Q. *Appl. Catal., B* **2013**, *140−141*, 1−8.
(54) Tian, W.; Yang, H. S.; Fan, X. Y.; Zhang, X. B. *J. Hazard. Mater.* **2011**, *188*, 105−109.
(55) Roy, S.; Viswanath, B.; Hegde, M. S.; Madras, G. *J. Phys. Chem. C* **2008**, *112*, 6002−6012.
(56) Wu, Z. B.; Jiang, B. Q.; Liu, Y.; Wang, H. Q.; Jin, R. B. *Environ. Sci. Technol.* **2007**, *41*, 5812−5817.
(57) Chen, L.; Li, J. H.; Ge, M. F. *Environ. Sci. Technol.* **2010**, *44*, 9590−9596.
(58) Shan, W. P.; Liu, F. D.; He, H.; Shi, X. Y.; Zhang, C. B. *Appl. Catal., B* **2012**, *115−116*, 100−106.
(59) Peng, Y.; Wang, C. Z.; Li, J. H. *Appl. Catal., B* **2014**, *144*, 538−546.
(60) Qi, G. S.; Yang, R. T.; Chang, R. *Appl. Catal., B* **2004**, *51*, 93−106.
(61) Liu, Z. M.; Zhang, S. X.; Li, J. H.; Ma, L. L. *Appl. Catal., B* **2014**, *144*, 90−95.
(62) Zhou, G. Y.; Zhong, B. C.; Wang, W. H.; Guan, X. J.; Huang, B. C.; Ye, D. Q.; Wu, H. J. *Catal. Today* **2011**, *175*, 157−163.
(63) Liu, Z. M.; Yi, Y.; Li, J. H.; Woo, S. I.; Wang, B. Y.; Cao, X. Z.; Li, Z. X. *Chem. Commun.* **2013**, *49*, 7726−7728.
(64) Zhang, L.; Pierce, J.; Leung, V. L.; Wang, D.; Epling, W. S. *J. Phys. Chem. C* **2013**, *117*, 8282−8289.
(65) Richter, M.; Trunschke, A.; Bentrup, U.; Brzezinka, K. W.; Schreier, E.; Schneider, M.; Pohl, M. M.; Fricke, R. *J. Catal.* **2002**, *206*, 98−113.
(66) Skalska, K.; Miller, J. S.; Ledakowicz, S. *Sci. Total Environ.* **2010**, *408*, 3976−3989.
(67) Huang, J. H.; Tong, Z. Q.; Huang, Y.; Zhang, J. F. *Appl. Catal., B* **2008**, *78*, 309−314.
(68) Xu, W. Q.; He, H.; Yu, Y. B. *J. Phys. Chem. C* **2009**, *113*, 4426−4432.
(69) Wu, Z. B.; Jin, R. B.; Wang, H. Q.; Liu, Y. *Catal. Commun.* **2009**, *10*, 935−939.